

## Research Article

# Research on an Ultrasonic Cutting Device Based on 0Cr18Ni9

San Hongjun ,<sup>1</sup> Yongxia Zhang,<sup>1</sup> Mingfang Chen ,<sup>1</sup> and Hao Wu<sup>2</sup>

<sup>1</sup>*Faculty of Mechanical and Electrical Engineering, Kunming University of Science and Technology, Kunming 650500, China*

<sup>2</sup>*College of Mechanical Engineering and Automation, Northeastern University, Shenyang 110819, China*

Correspondence should be addressed to Mingfang Chen; [mfchen111@sina.com](mailto:mfchen111@sina.com)

Received 8 April 2018; Revised 8 June 2018; Accepted 13 August 2018; Published 19 December 2018

Academic Editor: Rafał Burdzik

Copyright © 2018 San Hongjun et al. This is an open access article distributed under the Creative Commons Attribution License, which permits unrestricted use, distribution, and reproduction in any medium, provided the original work is properly cited.

For precision machining of 0Cr18Ni9, a two-dimensional ultrasonic cutting device is studied, which is composed of an elliptical ultrasonic vibration-working head and a two-dimensional high-power ultrasonic driving system. The working head is designed according to the size of the lathe tool post. The flange is designed in the nodal plane, and the ultrasonic oscillator is fixed in the flange plate, which can reduce the mechanical loss of vibration. The drive system can realize the linkage amplitude and synchronous control of the two arms. The speed of the synchronous frequency tracking is fairly fast, and the precision is satisfactory. The vibration shape of the working head can be arbitrarily set, and the vibration shape is stable. Through the cutting experiments of 0Cr18Ni9, the relationship between the speed of cutting line and the quality of cutting and the relationship between the vibration shape and the cutting quality, tool wear, and chip are all analyzed.

## 1. Introduction

With the rapid development of the automotive, aerospace, engineering machinery, and other industries, the demands of large plastic and high hardness parts are increasingly vigorous, which also contribute to the stainless steel, ceramics, composites, and hard alloy of difficult-to-machine materials that have been widely used [1]. By using traditional processing methods, these materials are generally difficult to be processed, such as large plastic material and high hardness material [2].

In comparison with conventional processing schemes, ultrasonic machining has salient advantages, such as small cutting force, low cutting heat, high surface quality of the workpiece, smooth chip removal, and high production efficiency  $i$  [3, 4]. Hence, it can be a potentially good solution to these difficult processes of materials, nonmetallic materials, and high surface quality requirements of parts machining problems [5, 6].

At present, the two-dimensional ultrasonic cutting is mainly through a single piezoelectric stack in a specific frequency band of two-dimensional vibration output, to assist the cutting [7–9]. The control of the two-dimensional mode is generally difficult; there are many restrictions on the

improvement of material-processing characteristics, and auxiliary cutting effect is limited [10].

For the precision machining of 0Cr18Ni9 that has been widely used in industrial engineering, in this paper, a 2D ultrasonic vibration cutting device is studied [11]. The proposed device can maintain long-term, stable, safe, and reliable operations. At the same time, in order to facilitate the analysis and performance improvement, the amplitude and phase of the two vibration arms can be precisely adjusted, and the two-dimensional vibration type can be set freely [12].

## 2. Processing Principle of Elliptical Ultrasonic Cutting

This scheme differs from traditional elliptical ultrasonic cutting mechanisms [6, 7]. The solution is to apply a high-power, accurate, and controllable elliptical ultrasonic vibration-assisted cutting method to the tool in the x-z feed plane, as shown in Figure 1. The auxiliary ultrasonic vibration frequency is adjustable in the range of 20–50 kHz. The processing characteristics of 0Cr18Ni9 material were analyzed by adjusting the vibration shape and vibration frequency of the ellipse.

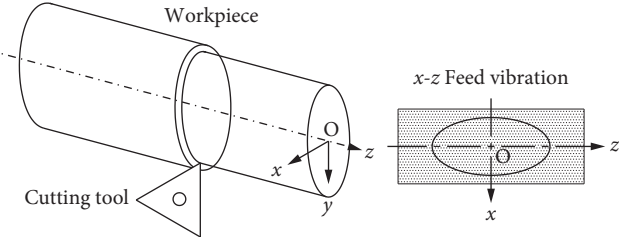


FIGURE 1: Elliptical ultrasonic cutting mechanism.

### 3. Elliptical Vibration Working Head

In order to facilitate the installation and popularization, the working head of the elliptical ultrasonic vibration is designed according to the size of the lathe tool post. The working head has two orthogonal vibrating arms; each arm is composed of an ultrasonic vibrator and a supporting mechanism. The designed scheme is shown in Figure 2 [11].

In order to improve the cutting performance and machining precision, the output amplitude of the vibrating arms should be retained between 5 and  $16\text{ }\mu\text{m}$  [11]. According to [13], the output displacement of the transducer is proportional to the driving power so that the driving voltage of the transducer cannot exceed AC 300 V.

In order to reduce the requirements of the cutting parameters, expand the processing range; the designed power of the system is 700 W, and the resonant frequency is 30 kHz [14, 15].

### 4. Design and Analysis of Vibration Mechanism

**4.1. Design and Analysis of Ultrasonic Vibration System.** The ultrasonic vibrator is composed of an amplitude transformer and a transducer, which is an important part of the vibrating arm. According to Figure 2, the ultrasonic vibrator can realize the vibration of the cutter head through the flexible hinge. Therefore, the success of the ultrasonic vibrator design will directly determine whether the cutter head is capable of outputting a specific vibration shape.

First of all, the analytical method is used to design the amplitude transformer and the transducer, and they are assembled into an ultrasonic vibrator, as shown in Figure 3. Then, we use ANSYS to implement optimization.

In the hexahedron element Solid95 with 20 nodes, the density, Young's modulus, and Poisson's ratio and other parameters were set as the inputs. The 3D solid model of the ultrasonic vibrator is then imported into ANSYS, and the 3D solid model of the ultrasonic vibrator is divided by the intelligent grid, which is shown in Figure 4.

In the frequency range of  $0\sim50\text{ kHz}$ , the modal of this designed model is analyzed and the results are shown in Figure 5. From the results of modal analysis, the third, fourth, fifth, tenth, eleventh, and fourteenth order are longitudinal vibrations, and the other various orders are included in the radial or longitudinal bending vibrations or torsional vibrations. Hence, the vibration mode does not meet the requirements of the system.

In particular, the following conclusions can be drawn from the results of the modal analysis shown in Figure 5.

In the third-order modal, the amplitude of the piezoelectric stack is too large, which may cause the mechanical loss of the piezoelectric stack, and the attenuation rate of the piezoelectric ceramic is also increased.

In the fourth-order modal, the amplitude of the connection between the transducer and the amplitude transformer is the largest.

In the fifth-order modal, the ultrasonic vibrator has a radial vibration at the top.

In the tenth-order modal, the amplitude of the piezoelectric stack is the largest and the ultrasonic vibrator has almost no vibration at the top.

In the fourteenth-order modal, the amplitude of the transducer is the largest and the amplitude of the ultrasonic vibrator's top is very small.

In the eleventh-order modal, the amplitude of the ultrasonic vibrator's top is the largest, and the flange plate and the piezoelectric stack have almost no vibration. Moreover, the resonance frequency of the ultrasonic vibrator is very close to that of the transducer and the amplitude transformer.

By setting the axial path of the amplitude transformer, the resonant-displacement distribution curve along the  $x$ -axis can be obtained, as shown in Figure 6. The green curve represents the amplitude of the front-end surface of the horn, and the pink curve represents the rear-end surface amplitude of the horn.

According to Figure 6, the displacement amplification factor  $M_p$  of the amplitude transformer can be analyzed. The half wavelength of the fundamental excitation signal is designed for the length of the amplitude transformer. The middle position of the amplitude transformer is the displacement of the nodal plane, and the design of the flange is the most reasonable. The flange plate is capable of providing support to the ultrasonic vibrator and can also reduce the influence of acoustic coupling.

The numerical analysis results shown in Figures 5 and 6 are compared with the results of the measurements, which are summarized in Table 1.

**4.2. Analysis of Elliptical Ultrasonic Vibration Working Head.** The cylinder of the working head is manufactured with 45# material, and the cutter head's material is 38CrMoAl. Their density, Young's modulus, and Poisson's ratio are set as the input, respectively. The three-dimensional solid model of the working head is imported into ABAQUS, and the modal analysis of the working head is carried out, where the results are shown in Figure 7.

From Figure 7, we can find that, in the fourth-order ( $f=2195.1\text{ Hz}$ ) and eighth-order ( $f=2465.2\text{ Hz}$ ) modal analysis results, the amplitude of the cutter tip is maximum and the other position is relatively small, even without vibration. Hence, the two-order vibration mode conforms to the requirements of the working head.

In the frequency range of  $0\sim40\text{ kHz}$ , the working head is the swept frequency. When the frequency of the excitation signal is  $18.764\text{ kHz}$  or  $30.285\text{ kHz}$ , the output power of the

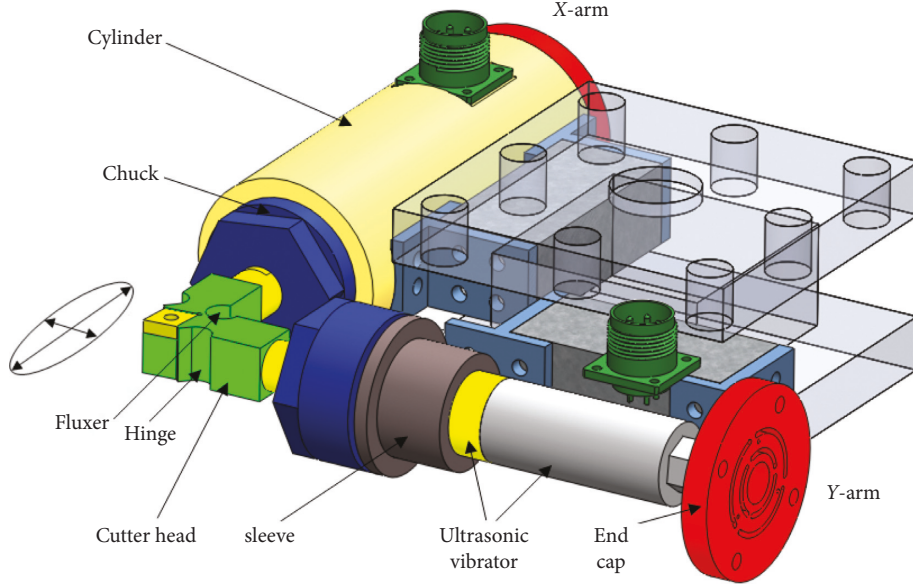


FIGURE 2: Scheme of elliptical ultrasonic vibration working head.

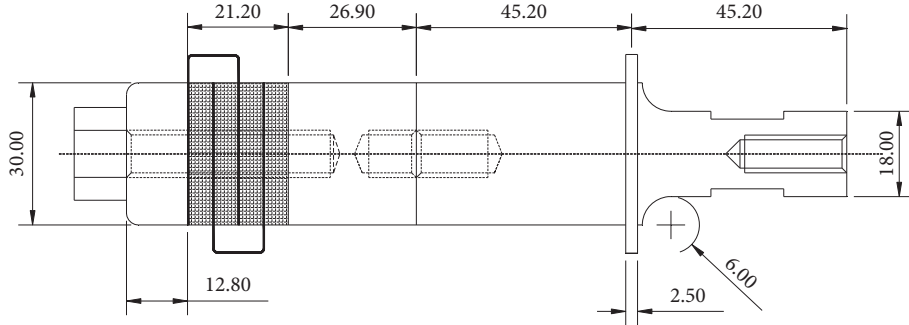


FIGURE 3: Design of the ultrasonic vibrator.



FIGURE 4: The mesh model of the ultrasonic vibrator.

drive system is relatively large. The two frequencies are very far from the frequencies of the working head's mode analysis but very close to the ultrasonic vibrator's mode analysis results of the fifth-order (18762 Hz) and the eleventh-order (30542 Hz).

## 5. Generation Mechanism of Vibration Trajectory

According to the design scheme of the working head (Figure 2), the vibration model is shown in Figure 8. The design excitation source for the two vibration arms and the tip can produce tiny elliptical vibration trajectory [10].

In Figure 8, the piezoelectric stack of the XY-arm is driven by a sinusoidal ultrasonic signal. Among them,  $\Delta x$

and  $\Delta y$  are the vibration displacements of the XY arms, respectively, such that

$$\Delta x = A \sin(2\pi ft) \quad \Delta y = B \sin(2\pi ft + \varphi), \quad (1)$$

where  $2\pi ft \in [0, 2\pi]$ ,  $f$  is the driving signal frequency,  $A$  and  $B$  are the amplitudes of the XY arms, and  $\varphi$  is the phase difference of the excitation signal. Formula (1) is the vibration equation of the cutter tip.

### 5.1. The Cutter Tip Trajectory Simulation

**5.1.1. Amplitude Linkage Adjustment.** When the phase difference  $\varphi$  values are  $\pi/6$ ,  $\pi/3$ , and  $\pi/2$ , the XY arms control amplitudes  $A$  and  $B$  are  $[16, 8]$ ,  $[12, 8]$ ,  $[8, 8]$ ,  $[8, 12]$ , and  $[8, 16]$   $\mu\text{m}$ , respectively. The simulation vibration trajectories are shown in Figure 9.

**5.1.2. Synchronous Phase Adjustment.** When the amplitudes of  $A$  and  $B$  are  $[16, 8]$ ,  $[8, 8]$ , and  $[8, 16]$   $\mu\text{m}$ , we adjust the XY arms phase difference  $\phi$  as  $\pi/6$ ,  $\pi/3$ ,  $\pi/2$ ,  $2\pi/3$ ,  $5\pi/6$ , and  $\pi$ , respectively; then the simulated vibration trajectories are shown in Figure 10.

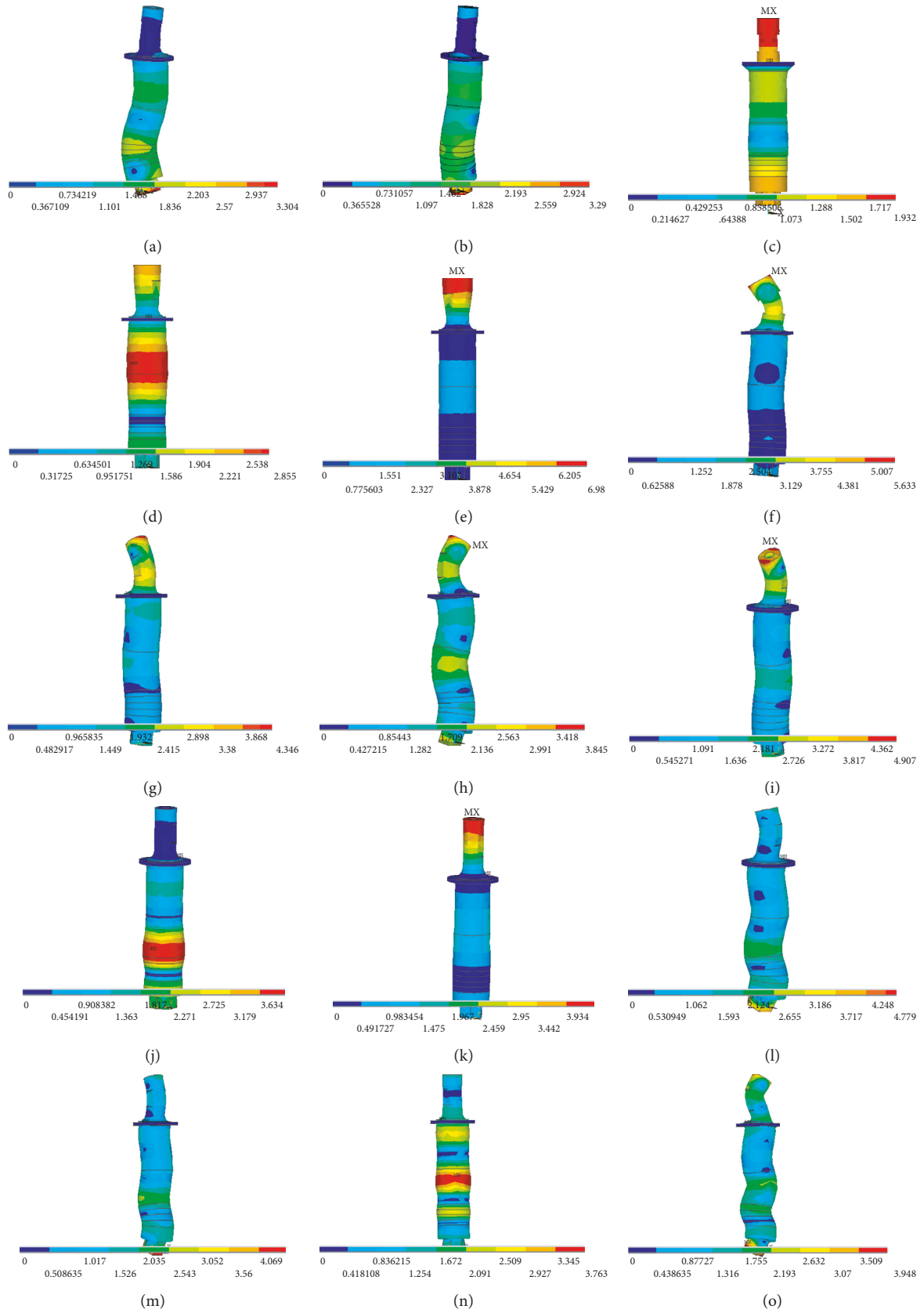


FIGURE 5: Modal analysis of the ultrasonic vibrator. (a)  $f_1 = 14431$  Hz, (b)  $f_2 = 14436$  Hz, (c)  $f_3 = 15661$  Hz, (d)  $f_4 = 16198$  Hz, (e)  $f_5 = 18762$  Hz, (f)  $f_6 = 23545$  Hz, (g)  $f_7 = 24304$  Hz, (h)  $f_8 = 26509$  Hz, (i)  $f_9 = 27239$  Hz, (j)  $f_{10} = 28438$  Hz, (k)  $f_{11} = 30542$  Hz, (l)  $f_{12} = 35953$  Hz, (m)  $f_{13} = 36148$  Hz, (n)  $f_{14} = 41549$  Hz, and (o)  $f_{15} = 43994$  Hz.

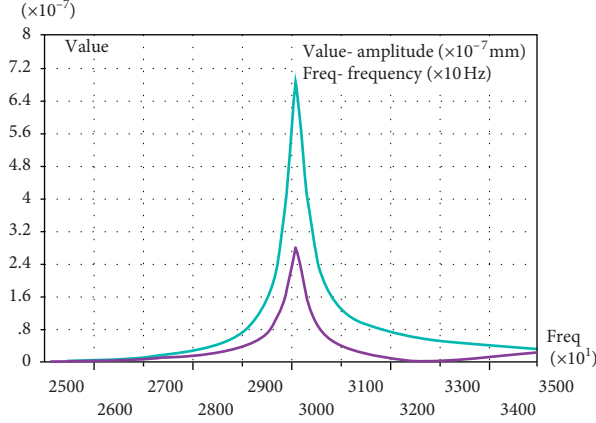


FIGURE 6: Distribution curve of axial displacement.

TABLE 1: Comparative results of analysis and measurements.

	Analytic value	Optimized value	Measured value	Analytical error (%)	Optimization analysis error (%)
Resonant frequency (kHz)	30	30.542	29.650	1.2	3
Amplification factor (Mp)	2.78	2.39	2.03	36.9	17.7

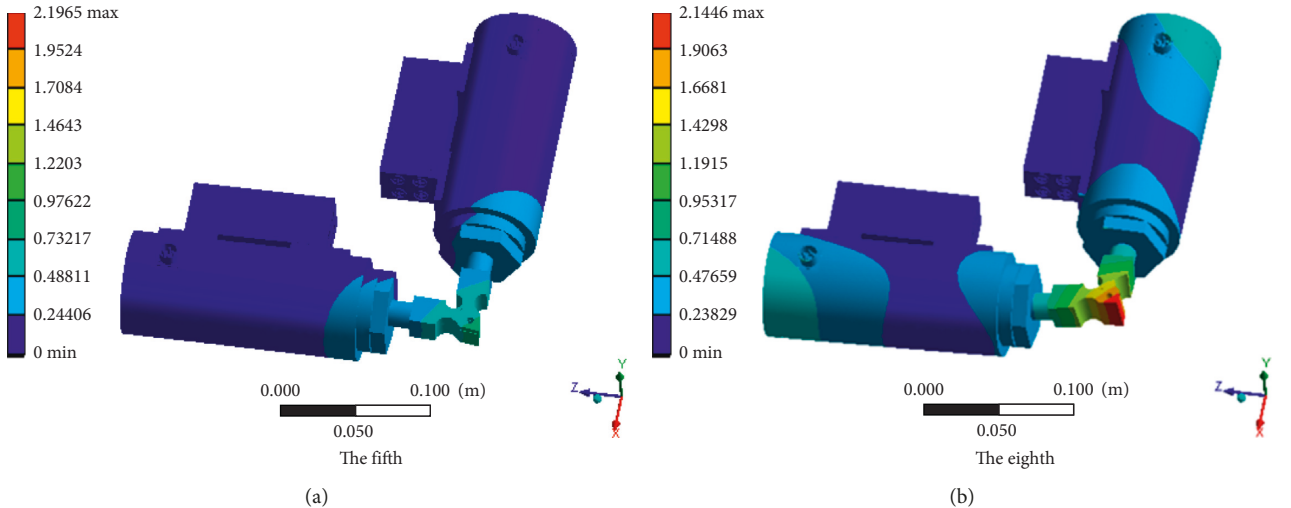


FIGURE 7: Modal analysis of elliptical ultrasonic vibration head. (a) The fourth and (b) the eighth.

**5.2. Two-Arms Linkage Amplitude Adjustment Control.** According to formula (1) and the trajectory simulation of two-arms amplitude linkage adjustment, it shows that when the phase angle  $\varphi$  is fixed, adjusting the amplitude  $AB$  of the two arms can change the cutter tip vibration trajectory.

In the literature [15], the output amplitude of the transducer is proportional to the power of the excitation signal. Since the load is almost a constant, the output amplitude of the transducer is positively related to the excitation voltage. Therefore, the amplitude regulation is realized by adjusting the excitation voltage.

Digital signal processor (DSP, TMS320F28335) output pins Epwm3A and Epwm3B are used to control the pulse width of the two drive signals so as to realize the precise and continuous adjustment of the excitation voltage. Finally, we complete the linkage control of  $A$  and  $B$  [15].

**5.3. Synchronous Phase Adjustment Control.** Synchronous phase adjustment control is usually difficult, which must meet the following two conditions [12]:

First, the driving signal must be the same clock source.

Second, assuming the initial phase of one arm is zero, the phase of the other arm is adjusted, and the mutual influence of phase adjustment and the dead time adjustment is considered.

The drive system uses the same clock source on the TMS320F28335 control board to ensure its synchronization. By formula (1), the synchronous phase adjustment trajectory simulation showed that when the amplitude  $AB$  of XY-arm is fixed, adjusting the phase difference  $\varphi$  can change the vibration trajectory of the cutter tip.

Taking the frequency signal of 18.73 kHz and 29.76 kHz as an example, the phase adjustment of the XY-arm is

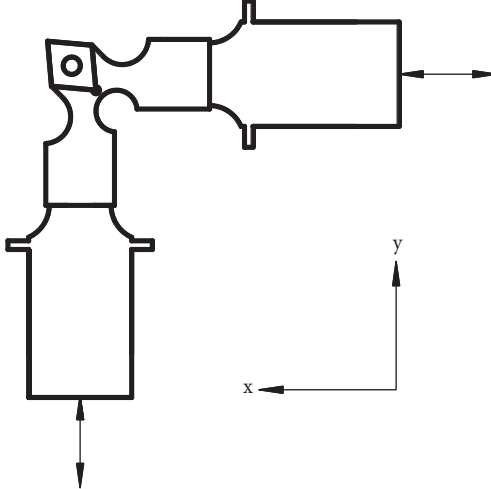
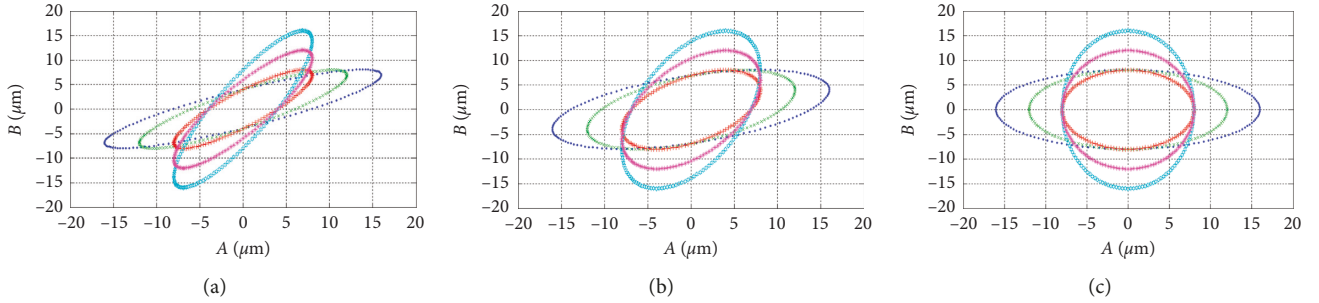
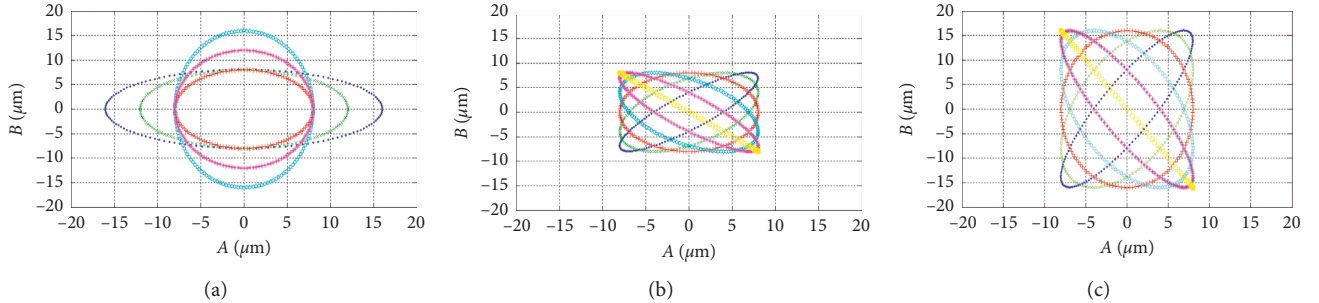


FIGURE 8: Elliptical ultrasonic vibration model.

FIGURE 9: Trajectory simulation of the amplitude of linkage adjustment: (a)  $\varphi = \pi/6$ . (b)  $\varphi = \pi/3$ . (c)  $\varphi = \pi/2$ . ·[16, 8]; ×[12, 8]; +[8, 8]; ☆[8, 12]; \*[8, 16].FIGURE 10: Trajectory simulation of the synchronous phase adjustment: (a)  $A = 16 \mu\text{m}$ ,  $B = 8 \mu\text{m}$ , (b)  $A = 8 \mu\text{m}$ ,  $B = 8 \mu\text{m}$ , and (c)  $A = 8 \mu\text{m}$ ,  $B = 16 \mu\text{m}$ . · $[\varphi = \pi/6]$ ; × $[\varphi = \pi/3]$ ; + $[\varphi = \pi/2]$ ; ☆ $[\varphi = 2\pi/3]$ ; \* $[\varphi = 5\pi/6]$ ; □ $[\varphi = \pi]$ .

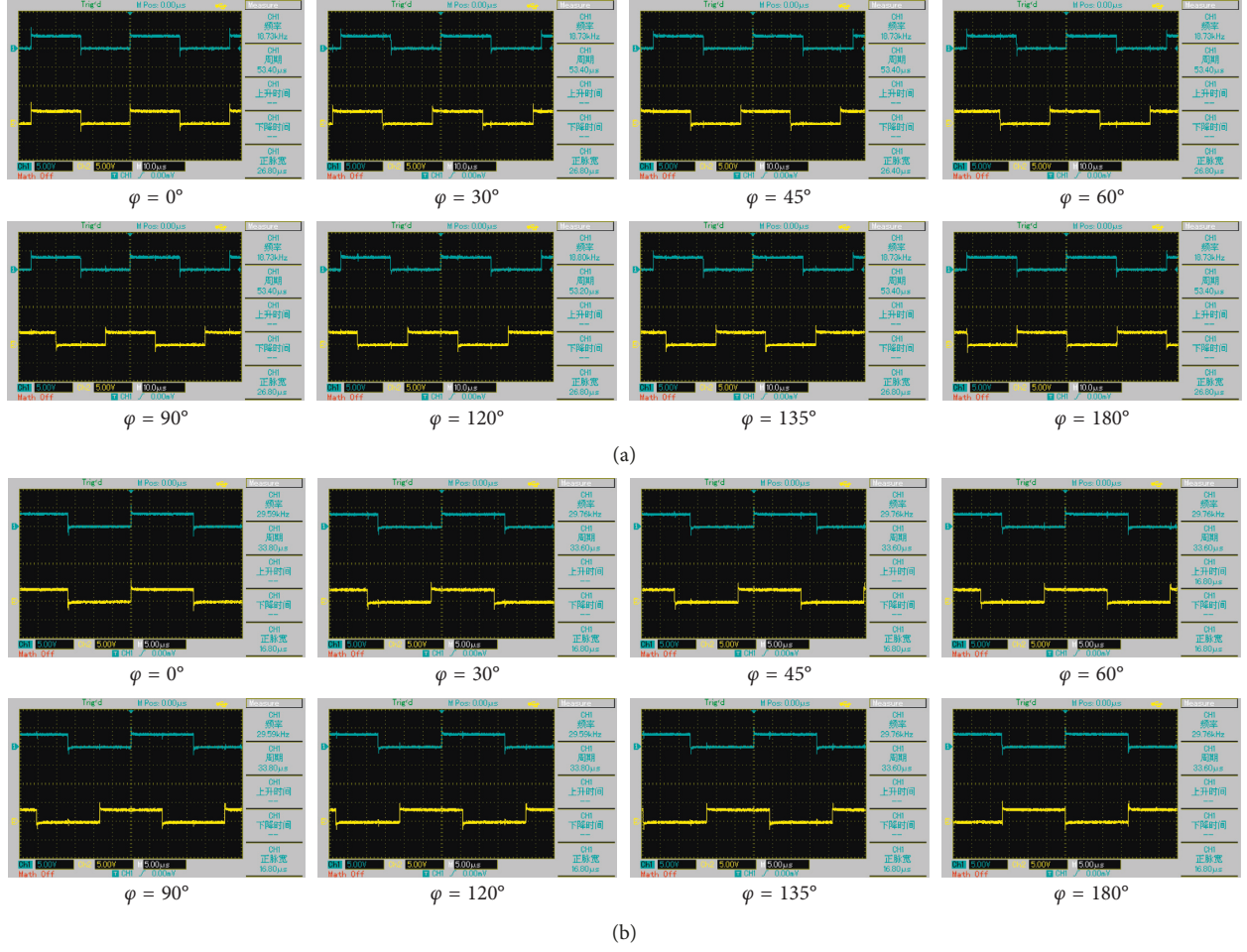
observed in the oscilloscope, which can be shown in Figure 11.

## 6. Synchronous Frequency-Tracking Control Scheme

The mechanical quality factor of the Sandwich piezoelectric transducer is small. For high-frequency vibrations, the elastic body of the transducer will heat up. The dielectric coefficient, equivalent capacitance, and leakage resistance of

the transducer can be changed with the increase in temperature. In addition, the change of cutting force, the change of contact constraint, etc., will result in the resonance frequency shift of about  $\pm 3$  kHz. When the frequency of the transducer is off resonance, the output amplitude of the driving arm will fall rapidly. In order to stabilize the output amplitude of the transducer, the drive system must have a fast frequency-tracking capability.

In this paper, the structure of the two vibration arms is completely symmetrical. In theory, the frequency tracking

FIGURE 11: DSP process of adjusting phase. (a)  $f = 18.73 \text{ kHz}$  and (b)  $f = 29.76 \text{ kHz}$ .

can choose any one arm for achieving tracking. But, in fact, it is difficult to ensure that the processing is fully consistent, and the parameters of each transducer are not completely consistent. Therefore, it is particularly important to design two-arm synchronous frequency-tracking scheme.

**6.1. Real-Time Frequency Tracking Circuit Based on 74HC4046.** The real-time frequency tracking control circuit based on 74HC4046 is shown in Figure 12. The phase signal of current and voltage is obtained by the high frequency inverter.

In Figure 12,  $V_{\text{TRANS}}$  is a high-frequency transformer, and it is used to extract the voltage phase.  $U_V$  (LM311) is a voltage comparator, the sinusoidal phase signal is converted into the square wave signal of the same frequency and the same phase to the 74HC4046's 3 pin.  $U_I$  extracts the current phase and converts it into a square-wave signal with the same frequency and the same phase, to the 74HC4046's 14 pin.

The work process of 74HC4046 PLL is as follows:

- (1) If the current phase (SIGIN) is ahead of the voltage phase (COMP\_IN), it must increase the frequency of the VCO so that its rising edge falls into the appropriate phase. At this time, the output of the PHC2 is set to a high level, the VCOIN is charged by the

loop filter, the VCOIN potential is raised, and the  $VCO_{\text{out}}$  frequency is increased. Once the rising-edge signal of COMP\_IN is detected, the output is turned into a high-impedance state, and the VCOIN voltage equals to the voltage of the loop filter. If the phase of the COMP\_IN is still lagging behind the SIGIN, then the PHC2 will continue to charge the VCOIN until they are in the same phase.

- (2) If the current phase (SIGIN) lags behind the voltage phase (COMP\_IN), when the VCO front-edge appears, the PHC2 output becomes low. The loop filter starts to discharge the VCOIN, the potential of VCOIN is decreased, and the output frequency of  $VCO_{\text{out}}$  is also decreased. If the voltage phase (COMP\_IN) is still ahead of the current phase (SIGIN), the PC2 phase detector will continue to discharge the VCOIN until the phase of the SIGIN and COMP\_IN is completely the same.
- (3) When the phase difference between the SIGIN and the COMP\_IN is zero, the PC2 phase detector outputs the high impedance state and the lock loop is realized.

In Figure 11, the C2 and R3 adopt the passive proportional integral filter. The integrator time constant not

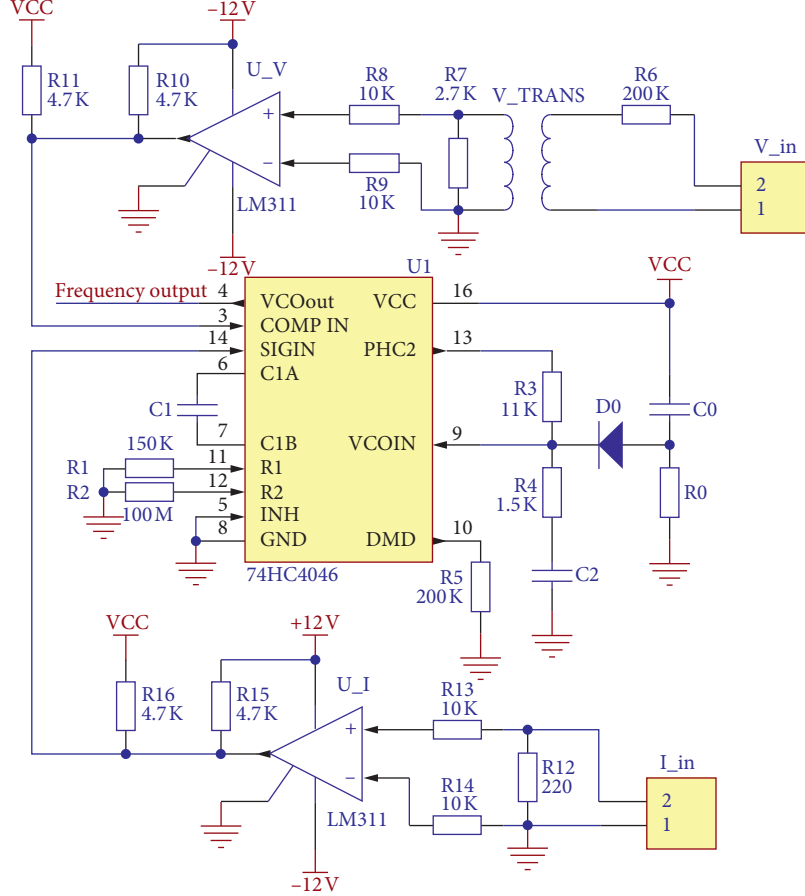


FIGURE 12: Frequency-tracking control circuit based on 74HC4046.

only limits the frequency-tracking range, but also directly influences the response speed of PLL frequency tracking. Moreover, the filter is a low-pass filter, and it can filter out the interference noise to some extent.

**6.2. Synchronous Frequency-Tracking Control Scheme.** This scheme can be used when their consistency is poor for the two ultrasonic vibrator and the vibration arms. This scheme mainly relies on the high-speed DSP to realize the fast search and operation so as to ensure the effective output of the vibration shape.

The implementation process of the control algorithm is as follows:

The first step is the no load full scan stage. The driving voltage of the ultrasonic vibrator is the maximum, that is  $U_x = U_y = 300 \text{ V}$ . The ultrasonic vibrator is the swept frequency. The intermediate frequency of  $f_{m0} = (f_x + f_y)/2$  is taken as the new resonance reference point for the drive system.

The second step is the try-cutting stage. Set  $U_x = U_y = 300 \text{ V}$  and  $f_{m0}$  as the center frequency, in the range of  $f_{m0} \pm 3 \text{ kHz}$ , to carry out the second frequency sweep and cutting at the same time. Take the frequency  $f_{mm}$  of the same (near) power as the new resonance point as shown in Figure 13.

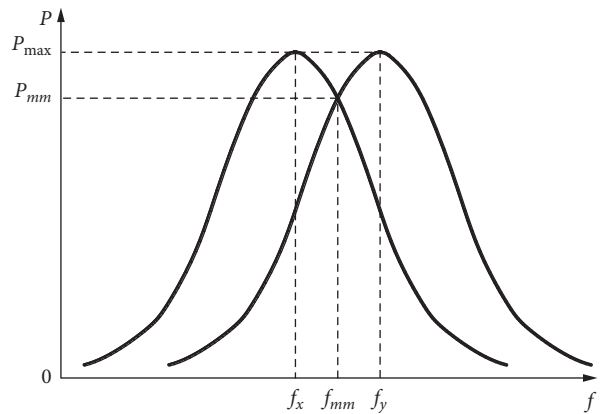


FIGURE 13: Equal-power resonance curve.

The third step is the formal cutting stage. The amplitude of the ultrasonic vibrator is proportional to the output power. According to the amplitudes of  $A$  and  $B$ , the powers  $P_{xs}$  and  $P_{ys}$  and amplitude ratio  $A:B$  can be calculated. Regulation of  $U_x$  makes  $P_x = (1 \pm \%5) P_{xs}$  and regulation of  $U_y$  makes  $P_x:P_y = (1 \pm \%5) \delta$ , until the end of the workpiece machining, otherwise returns to the second step.

The control algorithm of the scheme is shown in Figure 14.

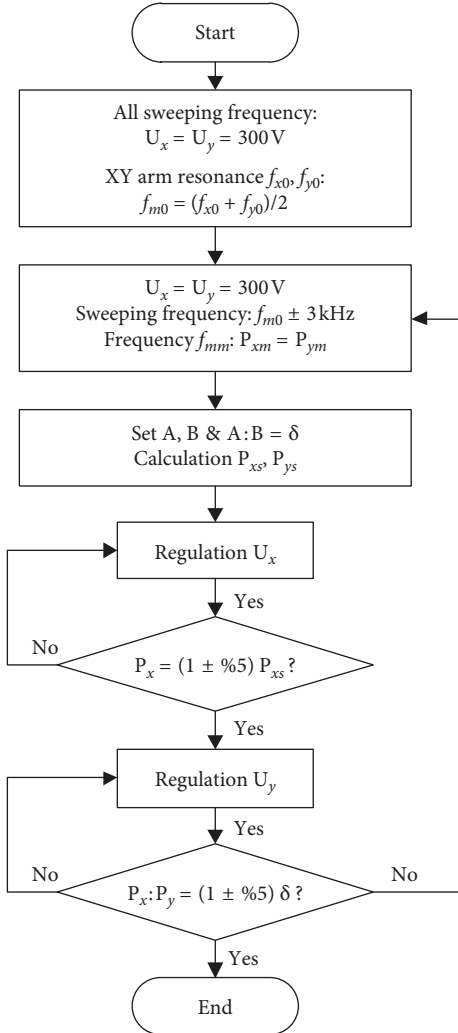


FIGURE 14: Synchronous frequency-tracking algorithm.

In the process of sweeping frequency, the load impedance  $R$  is a variable. In this paper, we can use  $P=UI$  to calculate  $P_x$  and  $P_y$ .

The control algorithm needs to run repeatedly in the DSP, which means that the real-time performance of the drive system may be poor, and the processing efficiency is low. However, if the material is uniform and the structure is simple without bubbles and other obvious defects, we do not need to repeat the frequency sweep. Thus, the processing efficiency will be much higher.

## 7. Cutting Test and Data Analysis

**7.1. Assembly of the 2D Ultrasonic Vibration Mechanism.** The scheme of the elliptical ultrasonic vibration working head is shown in Figure 1. According to this design scheme, the design, processing, and assembly of each component are completed as shown in Figure 15(a), and the working process of the working head is shown in Figure 15(b).

### 7.2. Vibration Shape Design and Cutting Quality Analysis

**7.2.1. Cutting Quality Analysis Based on Linear Speed.** The sample is a round bar of 0Cr18Ni9, with a diameter of 25 mm, the depth of cutting is 0.1 mm, and the feed rate is 0.1 mm/r. The corresponding relationship between the spindle speed of CA6140 and the cutting-line speed is shown in Table 2.

The amplitude of the XY-arm is set to 16  $\mu\text{m}$ , and the cutting tests are carried out according to the eight sets of line speed shown in Table 2.

The surface roughness of the workpiece can be obtained at different cutting-line speeds as shown in Figure 16. In different cases, the reasons for the different roughnesses are explained in detail in reference [2].

From Figure 16, the following facts can be summarized:

- (a) When one of the vibration arms is working, the surface quality of the workpiece is improved gradually with the increase of the cutting speed. When the cutting speed  $v=21.99 \text{ m/min}$ , the surface quality of the workpiece is optimal. Subsequently, the surface quality of the workpiece gradually deteriorates with the increase of the cutting-line speed.
- (b) When they are working independently, the surface quality of the work piece and the change trend of the cutting-line speed are the same, but the effect of the Y arm is more ideal.

If the ultrasonic vibration is applied, the cutting quality of the workpiece is the most obvious when the cutting speed is about 21.99 m/min. Therefore, further ultrasonic vibration cutting experiments are carried out in this line speed.

**7.2.2. Influence and Analysis of Vibration Shape.** When the phase difference  $\varphi = 90^\circ$ , through adjustment of the amplitude of XY-arm, we can produce different vibration shapes. One can observe the corresponding workpiece surface texture and roughness, which is shown in Figure 17.

Through the analysis of Figure 17, the following conclusions can be drawn:

- (a) When there is no ultrasonic vibration, the workpiece surface of three-dimensional cutting texture cross section is triangular, along the cutting direction parallel to each other.

The roughness of the workpiece surface is related to the difference of the peak and valley of the cutting texture. When the cutting tool is sharp, the average roughness is larger and vice versa.

- (b) According to the microscopic cutting-texture model and the average roughness value shown in Figures 17(b)–17(e), the following is drawn.

When the cutter tip shown in Figures 17(b) and 17(c) is applied, the elliptical vibration and cutting quality of the workpiece surface can be improved obviously. When the cutter tip shown in Figures 17(d) and 17(e) is used, the

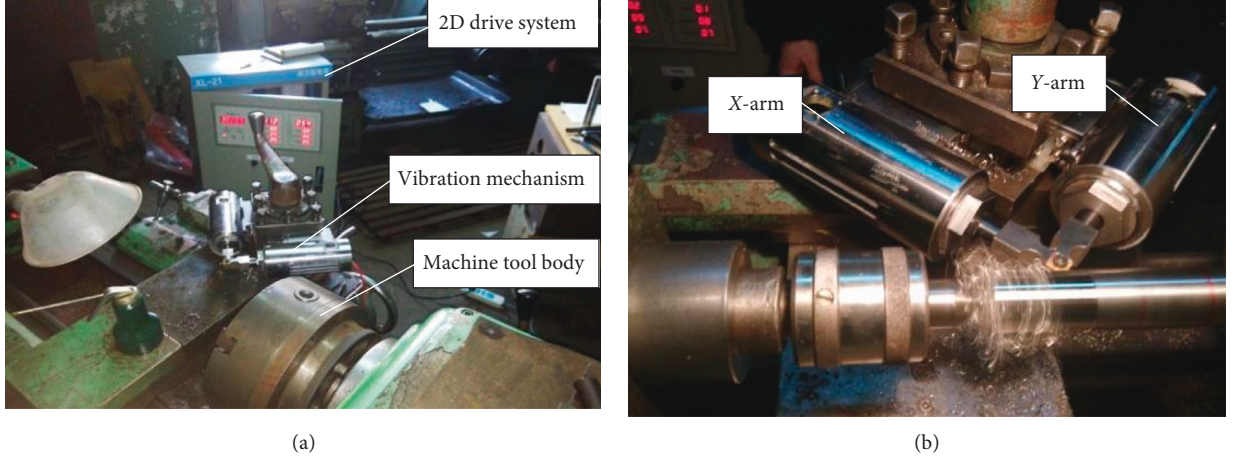


FIGURE 15: Assembly and process of mechanism. (a) Machine assembly and (b) processing.

TABLE 2: Spindle speed and cutting-line speed.

No.	1	2	3	4	5	6	7	8
Spindle speed (r/min)	180	220	280	355	450	500	560	630
Line speed (m/min)	14.14	17.28	21.99	27.88	35.34	39.27	43.98	49.48

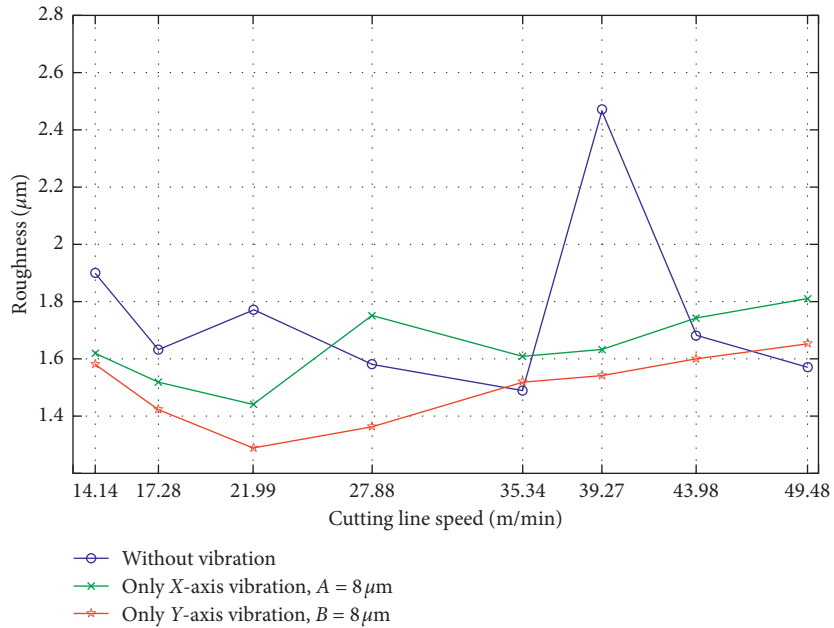


FIGURE 16: Surface roughness of workpiece at different line speeds.

circular vibration and cutting quality of the workpiece surface decreases and the larger amplitude and cutting quality decreases more obviously.

The phase adjustment is performed according to two kinds of elliptical vibration forms, i.e., Figures 17(b) and 17(c). The purpose is to find the optimal elliptical vibration shape.

**7.2.3. Vibration Shape Optimization Based on Phase Adjustment.** According to Figures 17(b) and 17(c) with the elliptic vibration form, we adjust the phase difference  $\phi$  and

set different elliptic vibration shapes. The detected roughness values are shown in Figure 18.

The result of Figure 18 shows that with the decrease of phase difference  $\phi$ , the surface quality of the workpiece is improved. However, when the elliptical vibration form of  $A < B$  is compared with  $A > B$ , the cutting quality is improved more obviously.

Therefore, concerning the surface quality of the work-piece, we find that the smaller the phase difference, the more optimized vibration shape.

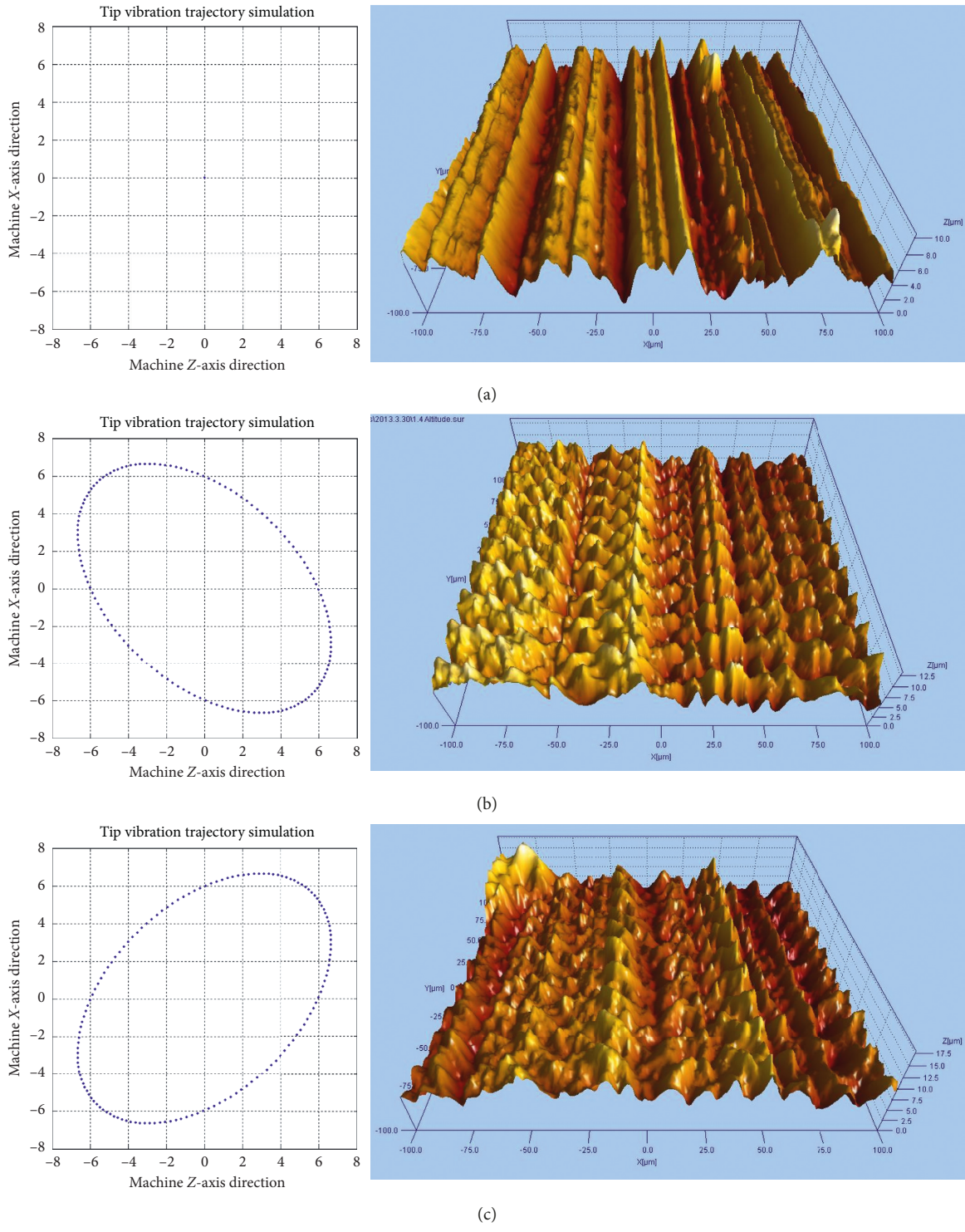


FIGURE 17: Continued.

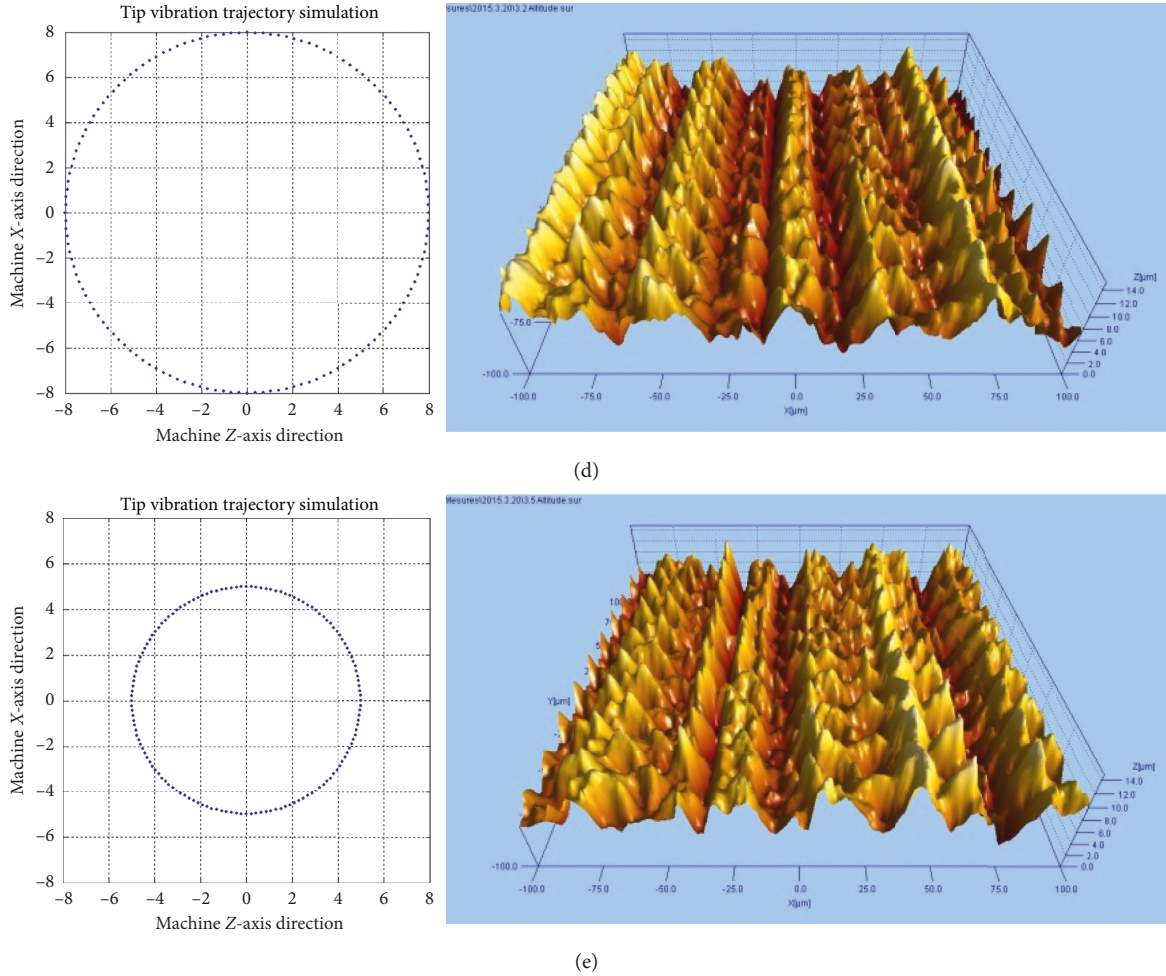


FIGURE 17: Influence of vibration mode on cutting quality: (a) no ultrasonic vibration,  $R_a = 1.80 \mu\text{m}$ ; (b)  $A = 16 \mu\text{m}$ ,  $B = 10 \mu\text{m}$ ,  $R_a = 1.39 \mu\text{m}$ ; (c)  $A = 10 \mu\text{m}$ ,  $B = 16 \mu\text{m}$ ,  $R_a = 1.29 \mu\text{m}$ ; (d)  $A = 16 \mu\text{m}$ ,  $B = 16 \mu\text{m}$ ,  $R_a = 2.17 \mu\text{m}$ ; (e)  $A = 10 \mu\text{m}$ ,  $B = 10 \mu\text{m}$ ,  $R_a = 1.88 \mu\text{m}$ .

**7.3. Effect of Vibration Shape on Tool Wear.** Based on the experimental results in Figure 18, the effect of optimized vibration shape on tool wear is further studied.

Cutting conditions are given as follows: workpiece material, workpiece diameter, spindle speed, cutting depth, and feed rate are the same as before and the surface cutting length is 157 meters. According to the various vibration shapes of Figure 18, we can observe their corresponding tool wear L as shown in Figure 19.

Through the analysis, we can get the following rules:

- (a) With the decrease of the phase angle, the tool wear is gradually increased
- (b) Under the same phase difference, the tool wear at  $A = 16 \mu\text{m}$  and  $B = 10 \mu\text{m}$  is worse than that of  $A = 10 \mu\text{m}$  and  $B = 16 \mu\text{m}$

**7.4. Influence of Vibration Shape on Chip Morphology.** When the phase difference  $\varphi$  is a constant at  $90^\circ$ , we adjust the amplitudes of AB. The optical lenses of the VHX-1000E three-dimensional display system are adjusted respectively to 3000 times and 20 times. The shape of the chip surface can be found in Figure 16.

From Figure 20 and the observations in the process, the following conclusions are drawn:

In Figure 20(a), no ultrasonic vibration is applied. Under optical lens 3000 times, the chip micro morphology is coiled texture of uniform motion in a straight line. Under 20 times of optical lens, the chip is of uniform shavings rolls, chip removal is difficult, and the chip has an easy winding cutter.

Figure 20(b) is with 3000 times of optical lens, the chip micro morphology is relatively deep and uneven. Under 20 times optical lens, the chip is short, broken, and relatively straight. In the process of machining, the chip is intermittent, smooth, and the chip has no winding cutter.

Figure 20(c) is with 3000 times of optical lens, the chip micro morphology is relatively shallow and uniform. Under 20 times optical lens, the chip is uniform wave-shaped and continuous. In the process of machining, the chip is smooth and there is no winding cutter, but the chip is longer.

Figure 20(d) is for 3000 times the optical lens, the chip micro morphology is relatively deep and uniform. In 20 times optical lens, the chip is uniform wave-shaped and continuous. In the process of machining, the chip is smooth and there is no winding cutter, but the chip almost constantly.

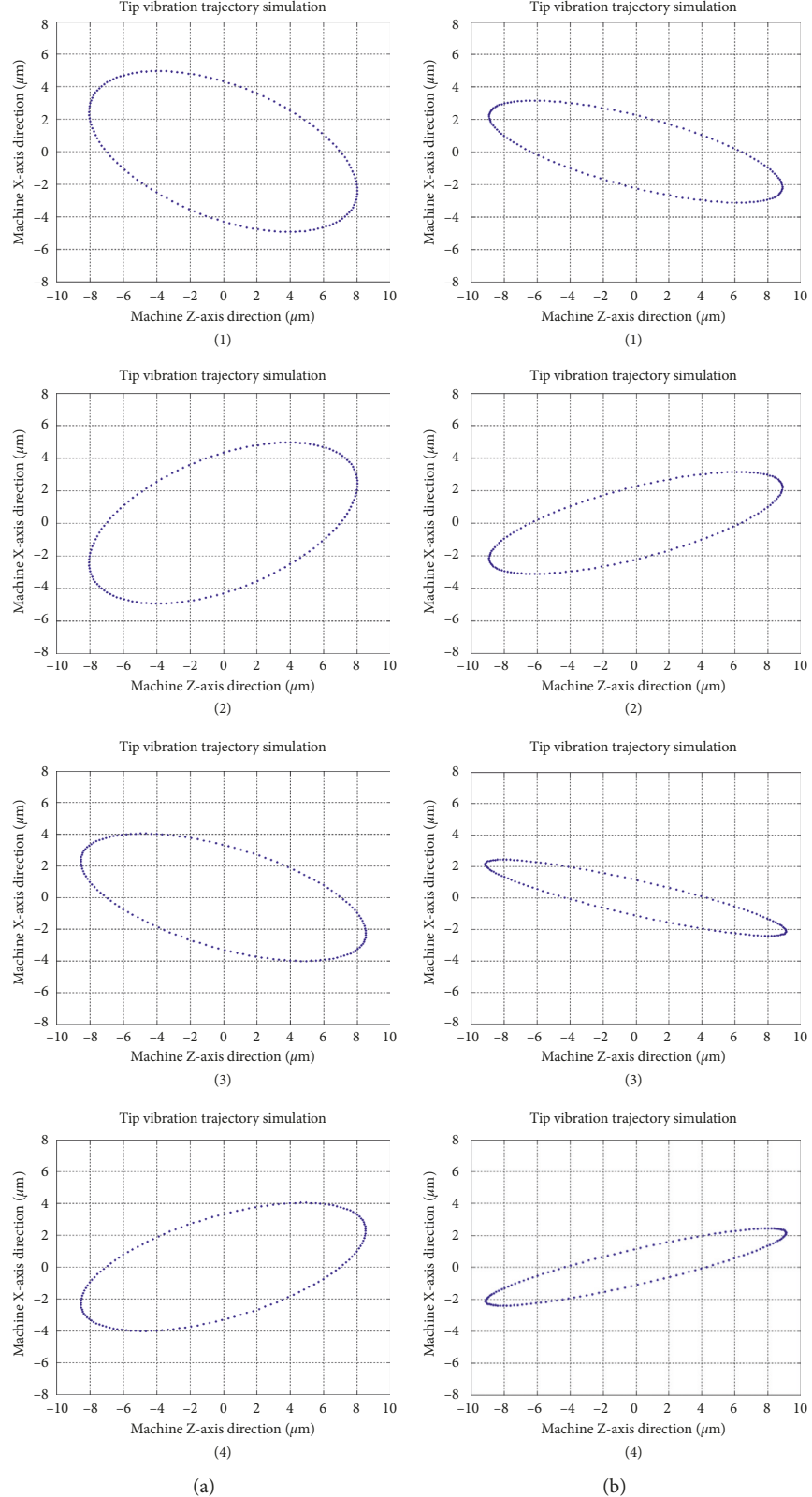


FIGURE 18: Effect of phase adjustment on cutting quality: (a)  $A = 16 \mu\text{m}$ ,  $B = 10 \mu\text{m}$ : (1)  $\varphi = 60^\circ$ ,  $\text{Ra} = 1.37 \mu\text{m}$ , (2)  $\varphi = 45^\circ$ ,  $\text{Ra} = 1.36 \mu\text{m}$ , (3)  $\varphi = 30^\circ$ ,  $\text{Ra} = 1.30 \mu\text{m}$ , and (4)  $\varphi = 15^\circ$ ,  $\text{Ra} = 1.27 \mu\text{m}$ . (b)  $A = 10 \mu\text{m}$ ,  $B = 16 \mu\text{m}$ : (1)  $\varphi = 60^\circ$ ,  $\text{Ra} = 1.25 \mu\text{m}$ , (2)  $\varphi = 45^\circ$ ,  $\text{Ra} = 1.18 \mu\text{m}$ , (3)  $\varphi = 30^\circ$ ,  $\text{Ra} = 1.17 \mu\text{m}$ , and (4)  $\varphi = 15^\circ$ ,  $\text{Ra} = 1.04 \mu\text{m}$ .

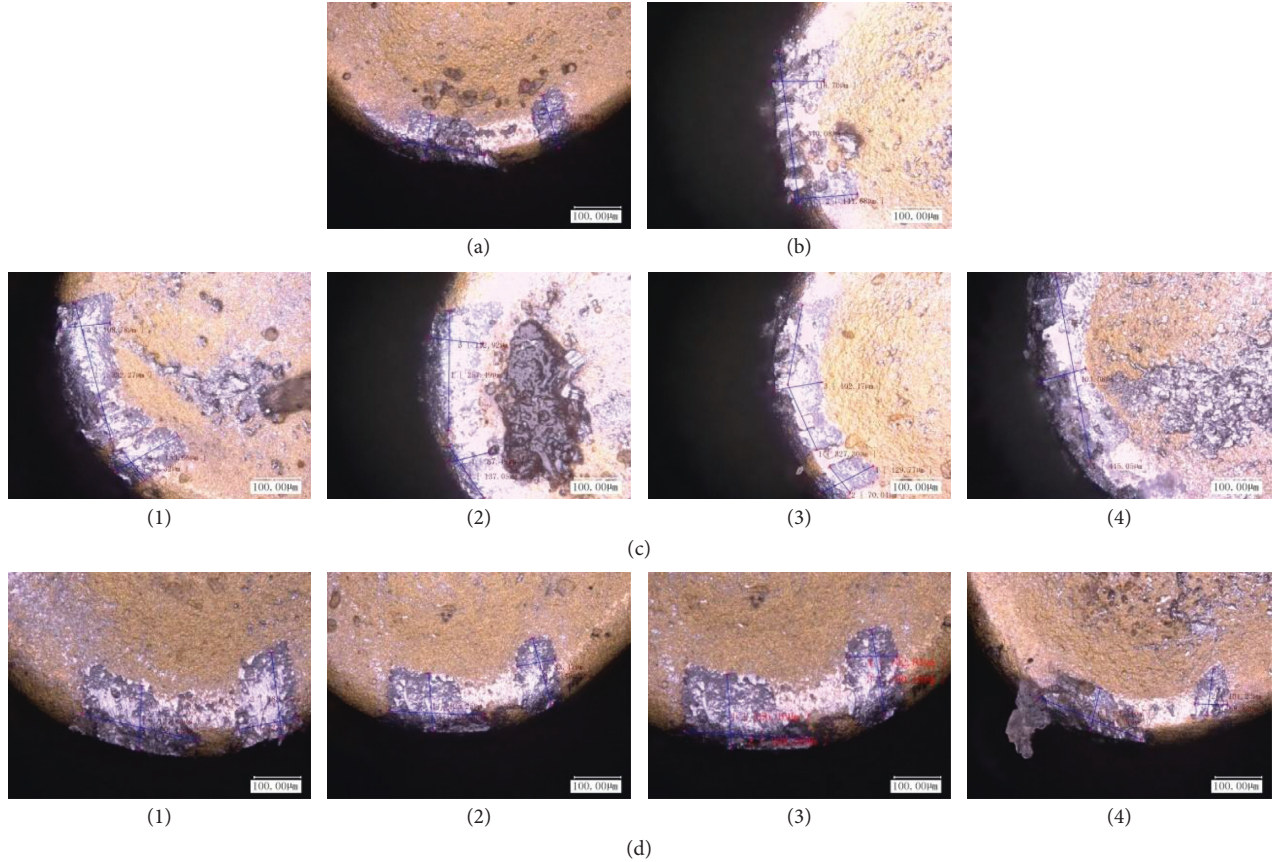


FIGURE 19: Influence of vibration shape on tool wear: (a)  $A = B = 10 \mu\text{m}$ :  $\varphi = 60^\circ$ ,  $L = 250.59 \mu\text{m}$ ; (b) no ultrasonic vibration:  $\varphi = 60^\circ$ ,  $L = 340.08 \mu\text{m}$ ; (c)  $A = 16 \mu\text{m}$ ,  $B = 10 \mu\text{m}$ : (1)  $\varphi = 60^\circ$ ,  $L = 386.59 \mu\text{m}$ , (2)  $\varphi = 45^\circ$ ,  $L = 394.54 \mu\text{m}$ , (3)  $\varphi = 30^\circ$ ,  $L = 397.34 \mu\text{m}$ , and (4)  $\varphi = 15^\circ$ ,  $L = 415.05 \mu\text{m}$ ; (d)  $A = 10 \mu\text{m}$ ,  $B = 16 \mu\text{m}$ : (1)  $\varphi = 60^\circ$ ,  $L = 283.35 \mu\text{m}$ , (2)  $\varphi = 45^\circ$ ,  $L = 287.32 \mu\text{m}$ , (3)  $\varphi = 30^\circ$ ,  $L = 371.50 \mu\text{m}$ , and (4)  $\varphi = 15^\circ$ ,  $L = 411.12 \mu\text{m}$ .

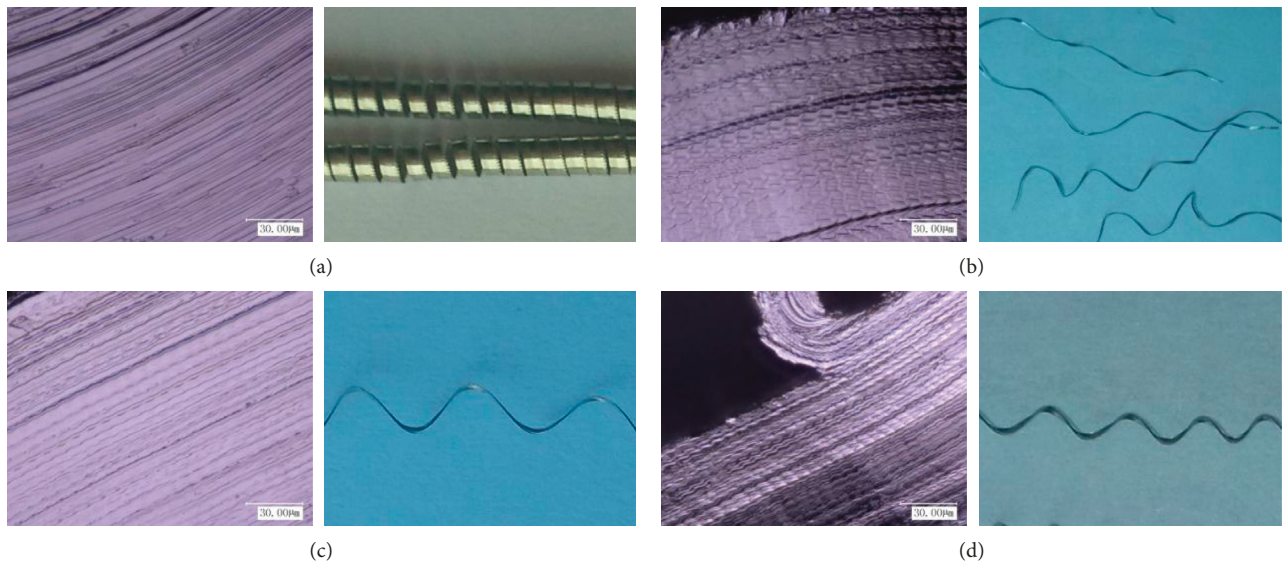


FIGURE 20: Chip morphology and appearance of chip: (a) no ultrasonic vibration; (b)  $A = 16 \mu\text{m}$ ,  $B = 10 \mu\text{m}$ ; (c)  $A = 10 \mu\text{m}$ ,  $B = 16 \mu\text{m}$ ; (d)  $A = 16 \mu\text{m}$ ,  $B = 16 \mu\text{m}$ .

## 8. Conclusion

Experiments show that the drive system vibration typeset has an obvious influence on the cutting effect; the synchronous frequency tracking is fast, tracking precision is high, and the output amplitude is stable.

Through the cutting test of 0Cr18Ni9, the influence of cutting line speed and ultrasonic vibration mode on the machining quality is studied, and the influence of the vibration mode on the surface quality, tool wear, and chip morphology are investigated.

The experimental results show that, compared with the conditions without ultrasonic vibration-assisted cutting, when the elliptical vibration mode is appropriate, the surface roughness of the workpiece is improved by 42%. Similarly, tool wear can be reduced by 17%. In addition, the cutting chips also continuously break into chips, which is very favorable for the discharge of cutting chips, and the processing continues.

## Data Availability

The data used to support the findings of this study are available from the corresponding author upon request.

## Conflicts of Interest

The authors declare that there are no conflicts of interest regarding the publication of this paper.

## References

- [1] D. Dornfeld, S. Min, and Y. Takeuchi, "Recent advances in mechanical micromachining," *CIRP Annals*, vol. 55, no. 2, pp. 745–768, 2006.
- [2] Y. Xu, P. Zou, H. Yu, S. Chen, Y. Tian, and X. Gao, "Comparative experimental research in turning of 304 austenitic stainless steel with and without ultrasonic vibration," *Proceedings of the Institution of Mechanical Engineers Part C Journal of Mechanical Engineering Science*, vol. 231, no. 15, pp. 2885–2901, 2017.
- [3] L. Xun and D. Zhang, "Experimental study on the unseparated ultrasonic elliptical vibration cutting," *Journal of Mechanical Engineering*, vol. 46, no. 19, pp. 177–182, 2010.
- [4] D. Lu, Q. Wang, Y. Wu, J. Cao, and H. Guo, "Fundamental turning characteristics of inconel 718 by applying ultrasonic elliptical vibration on the base plane," *Materials and Manufacturing Processes*, vol. 30, no. 8, pp. 1010–1017, 2015.
- [5] P. Zou, Y. Xu, H. Yu, M. Chen, and H. Wu, "Experimental investigation of ultrasonic vibration assisted turning of 304 austenitic stainless steel," *Shock and Vibration*, vol. 2015, Article ID 817598, 19 pages, 2015.
- [6] Q. Wang, Y. Wu, J. Gu, D. Lu, Y. Ji, and M. Nomura, "Fundamental machining characteristics of the in-base-plane ultrasonic elliptical vibration assisted turning of inconel 718," *Procedia CIRP*, vol. 42, pp. 858–862, 2016.
- [7] Z. Yin, Y. Fu, J. Xu, H. Li, Z. Cao, and Y. Chen, "A novel single driven ultrasonic elliptical vibration cutting device," *International Journal of Advanced Manufacturing Technology*, vol. 90, no. 9–12, pp. 3289–3300, 2017.
- [8] A. A. G. Bruzzone, H. L. Costa, P. M. Lonardo, and D. A. Lucca, "Advances in engineered surfaces for functional performance," *CIRP Annals*, vol. 57, no. 2, pp. 750–769, 2008.
- [9] G. Kim and B. Loh, "Machining of micro-channels and pyramid patterns using elliptical vibration cutting," *International Journal of Advanced Manufacturing Technology*, vol. 49, no. 9–12, pp. 961–968, 2010.
- [10] C. Nath, M. Rahman, and K. S. Neo, "A study on ultrasonic elliptical vibration cutting of tungsten carbide," *Journal of Materials Processing Technology*, vol. 209, no. 9, pp. 4459–4464, 2009.
- [11] M.-F. Chen, P. Zou, Z.-X. Yu, and Y.-T. Zhao, "Study on the cutting mechanism of power type elliptic ultrasonic vibration," *Mechanical Design and Manufacturing*, vol. 277, no. 3, pp. 8–11, 2014.
- [12] T. Sun, M. Chen, Q. Sun, and Y. Zhang, "Research of elliptic ultrasonic vibration mechanism," *Applied Mechanics and Materials*, vol. 789–790, pp. 156–159, 2015.
- [13] M.-F. Chen, P. Zou, Y. He, H. Wu, and Y.-X. Zhang, "Study on optimization BUCK model used in elliptic ultrasonic power cutting driving device," *China Mechanical Engineering*, vol. 26, no. 1, pp. 18–24, 2015.
- [14] M. Chen and P. Zou, "Based on STA9800VT high frequency slight vibration test system design and analysis," *Instrument Technique and Sensor*, vol. 360, no. 1, pp. 23–26, 2013.
- [15] M.-F. Chen, P. Zou, G. Han, and B.-M. Hou, "Research on nc auxiliary ultra-precision positioning work platform," *Journal of Northeastern University (Natural Science Edition)*, vol. 34, no. 6, pp. 875–878, 2013.

